Cell Metabolism, Volume *31*

Supplemental Information

Mitochondria-Endoplasmic Reticulum Contacts in Reactive Astrocytes Promote Vascular Remodeling

Jana Göbel, Esther Engelhardt, Patric Pelzer, Vignesh Sakthivelu, Hannah M. Jahn, Milica Jevtic, Kat Folz-Donahue, Christian Kukat, Astrid Schauss, Christian K. Frese, Patrick Giavalisco, Alexander Ghanem, Karl-Klaus Conzelmann, Elisa Motori, and Matteo Bergami

Legends to Supplemental Figures

Figure S1. Related to Figure 1. Characterization of organelle distribution across astrocytic territories *in vivo*. (A) Left panel: example (confocal z-projection) of a cortical astrocyte transduced with an astrocyte-specific virus encoding for mitoRFP. The location of one astrocytic end-foot and soma (S) are depicted. Right panel: rendered image of mitoRFP (following deconvolution) of a single stack and the corresponding immunoreactivity for CD31 of nearby microvessels. Low panels shows zooms of each respective yellow boxed region. Bars, 15 µm. **(B)** Left panel: example (confocal z-projection) of a cortical astrocyte transduced with an astrocyte-specific virus encoding for ER-GFP. The location of astrocytic end-feet and soma (S) are depicted. Right panel: rendered image of ER-GFP (following deconvolution) of a single stack and the corresponding immunoreactivity for CD31 of nearby microvessels. Low panels shows zooms of each respective yellow boxed region. Bars, 15 µm. **(C)** Example of a cortical astrocyte transduced with an astrocyte-specific AAV encoding for a lysosomal marker (Emerald-Lamp1) and cytosolic mCherry. The location of astrocytic territories including end-foot, branches/branchlets and soma (S) is depicted. Immunostaining for CD31 shows the presence of nearby microvessels. The right panel shows the Emerald-Lamp1 channel reporting on the distribution of lysosomes. Bar, 15 µm. **(D)** Zooms (surface rendered) of the boxed areas shown in **C**. Bar, 5 µm. **(E)** Example of a cortical astrocyte transduced with an astrocyte-specific AAV encoding for a peroxisomal marker (mCherry-Perox) and cytosolic BFP. The location of astrocytic territories including end-foot, branches/branchlets and soma (S) is depicted. Immunostaining for CD31 shows the presence of nearby microvessels. The right panel shows the mCherry-Perox channel reporting on the distribution of peroxisomes. Bar, 15 µm. **(F)** Zooms (surface rendered) of the boxed areas shown in **E**. Bar, 5 µm. **(G)** Example of a portion of cortex in a brain section from tamoxifen-induced Glast::CreER^{T2} x R26$^{LSL\text{-}tdTomato}$ mice immunostained for the endothelial marker CD31, showing the extent of perivascular end-feet wrapping around the vasculature. Bar, 50 µm. **(H)** EM picture of a similar specimen as in **G** following immuno-gold processing against RFP. A superimposed red shadow identifies the location of the perivascular end-foot enriched in gold particles. The zoom

on the right illustrates the localization of gold particles within the end-foot surrounding the basal lamina.

Figure S2. Related to Figure 2. Remodeling of astrocyte mitochondrial and ER networks following SW-injury. (A) Example of brain section from tamoxifen-induced hGFAP::CreER^{TM} x R26$^{LSL\text{-}mitoYFP}$ mice immunostained for the astrocytic marker S100β. Left inset: zoom of a single S100β+/mitoYFP+ astrocyte. Right inset: quantification of recombination efficiency in the cortex. Bars, 20 µm. **(B)** Examples of mitoYFP+ astrocytes in control (uninjured) and injured conditions (SW 7 days, astrocyte proximal to the lesion track) showing the presence of CD45+ leukocytes (labeled in cyan) after SW injury. Bars, 15 µm. **(C)** Examples of a mitoYFP+ (left) and an ER-GFP+ (right) astrocyte following injury (SW 7 days) showing co-labeling for the endothelial marker CD31. Zooms of the boxed regions depict the end-foot. Bar, 20 µm. **(D)** Quantification of astrocytic mitochondrial mass (total mitoYFP volume per astrocyte) in control (uninjured conditions, time 0) or following stab-wound injury (SW) at 7 and 28 days. Mitochondrial mass was normalized to that of control astrocytes at time 0. N= 22 (time 0), 32 (time 7 days) and 29 (time 28 days) astrocytes obtained from 3 different mice for each time point (one-way ANOVA followed by Kruskal-Wallis test). **(E)** Density of mitoYFP+ signal in peripheral branches of resting or reactive astrocyte at the indicated conditions (n≥ 33 astrocytes obtained from 3 mice/condition) (one-way ANOVA followed by Kruskal-Wallis test). **(F)** Scheme depicting the approach utilized for FACS and proteomic analysis of astrocytes following SW-injury. **(G)** Heat maps of normalized LFQ (label-free quantification) intensities of detected proteins regulating mitochondrial fission and fusion dynamics at the indicated time points after injury and color-coded according to their z-score (n= 6 mice per time point). **(H)** Heat maps of normalized LFQ (label-free quantification) intensities of detected proteins associated to mitochondrial biogenesis (Tfam and Nrf1) as well as with mitochondrial mass (Timm and Tomm proteins) (n= 6 mice per time point). Significant changes ($-\log_{10}$ of the *p*-value ≥1.3) are indicated with an asterisk. **(I)** Examples of a reconstructed ER-GFP astrocyte

(same as Figure 2J) following volume masking, segmentation of the indicated compartments (end-feet, soma and branches) and subsequent fractionation of the ER-GFP signal in each of these compartments to obtain the signal densities displayed in panel **L**. Bar, 20 µm. **(J)** Quantification of vessel diameter in the same dataset utilized to examine the ER-GFP perivascular g-ratio of Figure 2K. The plot shows data collected during a time course ranging from time 0 (uninjured) to 28 days after injury (n≥ 35 vessels/time-point; nonparametric Kruskal-Wallis test). **(K)** 3D examples of ER-GFP labelled reactive astrocytes at 7 and 28 days post-SW. Volume segmentation into end-feet (according to direct contact with the labelled vasculature), soma and branches is shown in different colors. Lower panels depict the ER-GFP signal density in pseudocolors. A zoom of a perivascular end-foot is shown. Bars, 10 µm. **(L)** Quantification of the fractional ER-GFP signal density across the three indicated astrocytic compartments in uninjured (n= 15 cells, 3 mice) or injured (7 days, n= 13 cells, 3 mice; 28 days, n= 22 cells, 2 mice) astrocytes. **(M)** Quantification of ER-GFP total volume per astrocyte. Right graph: average number of end-feet for the analysed ER-GFP expressing astrocytes as in **L** (one-way ANOVA followed by Dunn's post-hoc test). *, $p < 0.05$, **, $p < 0.01$, ***, $p < 0.001$.

Figure S3. Related to Figure 3 and 4. Label-free proteomic analysis of reactive Mfn2^{cKO} and Mfn1^{cKO} astrocytes responding to SW-injury. (A) Scheme showing the genotyping approach used for validating the conditional knock-out of *Mfn1* and *Mfn2* in cortical astrocytes *in vivo*. **(B)** Genotyping of isolated cortices from tamoxifen-induced Mfn1^{cKO}, Mfn2^{cKO} and relative control littermates (Mfn1^{WT} and Mfn2^{WT}). The upper gels report on the genotyping protocol to detect wild-type and floxed alleles for each gene, while the lower gels report on the deletion (knock-out) band originating from recombined astrocytes. **(C)** Volcano plot of Mfn2^{cKO} reactive astrocytes (~3280 detected proteins, ~2500 quantified) showing their relative expression levels (log_2 fold change) compared to reactive Mfn2^{WT} (Ctrl) astrocytes obtained from tamoxifen-induced littermates. Proteins with a *p*-value $\leq$ 0.05 (i.e. $\geq$ 1.3 on the $-log_{10}$

scale) are considered significant. Proteins annotated in the Mitocarta 2.0 are outlined in red (n= 4 $Mfn2^{cKO}$ mice and 3 Ctrl mice). **(D)** Heat map of normalized LFQ intensities of astrocytic markers of reactivity identified in our proteomics dataset and color-coded according to their z-score. Significant changes ($-\log_{10}$ of the *p*-value ≥1.3) are indicated with an asterisk at the beginning of each row. **(E)** Plot showing the increased expression of MFN2 in sorted $Mfn1^{cKO}$ astrocytes at 28 days following injury. The left column reports on the distribution of the whole proteome in $Mfn1^{cKO}$ astrocytes. MFN2 expression is significantly up-regulated under these conditions (**, p value <0.01). **(F)** Ingenuity Pathway Analysis (IPA) of the proteome of $Mfn2^{cKO}$ and $Mfn1^{cKO}$ astrocytes disclosing significantly up- (red) and down-regulated (blue) pathways (bars indicate the $-\log_{10}$ of the p-value starting with a minimum cut-off of 1.3). Besides several shared pathways, $Mfn2^{cKO}$-specific up-regulated pathways included Wnt/β-catenin, Insulin Receptor Signaling, Methylmalonyl and 2-oxanobutanoate Degradation and Ca^{2+} Transport. Of the down-regulated pathways, OXPHOS and Regulation of eIF4 and p70S6K Signaling appeared to be specific for $Mfn2^{cKO}$ astrocytes (n= 4 $Mfn2^{cKO}$ mice, 4 $Mfn1^{cKO}$ mice and 3 Ctrl mice). **(G)** Heat maps of normalized LFQ (label-free quantification) intensities of detected OXPHOS complex subunits (complexes I to V) color-coded according to their z-score (n= 4 $Mfn2^{cKO}$ mice, 4 $Mfn1^{cKO}$ mice and 3 Ctrl mice). Significant changes ($-\log_{10}$ of the *p*-value ≥1.3) are indicated with an asterisk at the beginning of each row. **(H)** Heat maps of normalized LFQ intensities of detected proteins associated to mitochondrial stress responses color-coded according to their z-score. Significant changes ($-\log_{10}$ of the *p*-value ≥1.3) are indicated with an asterisk at the beginning of each row.

Figure S4. Related to Figure 4. Mitochondrial network changes in astrocytes following deletion of *Mfn2* or *Mfn1*. (A) Surface rendering examples of mitochondrial morphologies detected in Ctrl, $Mfn2^{cKO}$ and $Mfn1^{cKO}$ resting astrocytes (i.e., uninjured animals). Yellow arrowheads point to the soma. Zooms of the boxed areas depict the predominant network morphology in peripheral processes. Bar, 15 µm. **(B)** Examples of ER-RFP+ resting astrocytes (i.e., in uninjured mice) showing the distribution of the ER in relation to CD31 immunostaining.

Yellow arrowheads point to the soma. Zooms of the boxed regions depict the end-feet. Bar, 20 µm. **(C)** Top panels: 3D volume reconstructions showing Ctrl, $Mfn2^{cKO}$ and $Mfn1^{cKO}$ astrocytes (arrowheads point to the soma) surrounding dextran-labelled vessels at 7 days post-SW. Bottom pictures show single-stack views highlighting the extent of perivascular mitochondria for each condition. Bar, 20 µm. **(D)** EM pictures of astrocytic end-feet in $Mfn2^{WT}$ and $Mfn2^{cKO}$ mice at 4 weeks post-SW, showing the extent and morphology of perivascular mitochondria. Images were taken in proximity to the lesion track. Insets depict zooms of mitochondrial cristae. EC: endothelial cell; BL: basal lamina. Bars, 500 nm. **(E)** Details of astrocytic end-feet showing the morphology of ER tubules in $Mfn2^{WT}$ and $Mfn2^{cKO}$ mice. Bar, 500 nm. **(F)** Quantification of the indicated ultrastructural parameters in $Mfn2^{WT}$ (n= 18 vessel cross-sections from 3 mice) and $Mfn2^{cKO}$ perivascular end-feet (n= 24 vessel cross-sections from 3 mice; non-parametric Mann-Whitney t-test). ***, $p < 0.001$.

Figure S5. Related to Figure 5. Mitochondrial and cytosolic Ca^{2+} dynamics in $Mfn2^{cKO}$ astrocytes. (A) Schematic illustrating the experimental protocol used to transduce astrocytes in hGFAP-TVA mice with an EnvA-RABV encoding for the photoactivatable mito-GFP sensor (mito-PA-GFP). Seven days after virus delivery, 2PLSM in fresh brain slices was utilized to assess mitochondrial fusion dynamics in transduced cortical astrocytes. ROI photoactivation in selected astrocytic processes was achieved by laser illumination in the UV range (840 nm at 10% of laser power for 10 seconds), which resulted in bright GFP emission. Time-lapse was performed to follow the fate of the photoactivated mitochondria, which in case of fusion occurring would lead to sudden appearance in the GFP channel of “new” (non-photoactivated) mitochondria, with concomitant dilution of GFP signal intensity in initially photoactivated mitochondria undergoing fusion. **(B)** Example of a mito-PA-GFP-expressing astrocyte surrounded by small and large vessels (indicated by yellow arrows) recognizable by the characteristic mitochondrial outlining into tube-like structures. The laser intensity utilized for GFP detection (920 nm) was slightly increased during preliminary acquisition to identify the

morphological appearance of weak PA-GFP-expressing mitochondria along processes and putative end-feet. Boxed areas point to selected ROIs prior photoactivation. Panels on the right depict selected time points of the z-scan time-lapse which was carried out for at least 1 hour following initial photoactivation (for time-lapse, the laser was tuned back to 920 nm with intensity lower than 1%, one z-scan every 3 minutes). Following z-stack image registration, direct comparison of GFP signal between time points was examined manually. Arrowheads point to fusion events, which are recognizable by the abrupt decrease in GFP intensity in photoactivated mitochondria due to GFP dilution into the newly appearing (fusing) mitochondria. Mitochondria that were identified for simply moving away from the photoactivated ROI and did not satisfy these parameters were not considered in our quantification. Bar, 20 µm. **(C)** Quantification of fusion rates in astrocytic end-feet and branches over the course of 1 hour of imaging (n= 17 astrocytes from 4 mice). Note the overall low fusion rate under resting conditions in both branches and end-feet. **(D)** Schematic showing AAV-mediated cytoGCaMP6f expression in astrocytes followed by 2PLSM in slices and subsequent AstroSparks analysis. **(E)** Example of cytoGCaMP6-expressing astrocytes in brain slice following AstroSparks processing and ROI detection (ROIs in end-feet are depicted in white). Right panels depict ROI traces and corresponding raster plots. Bar, 20 µm. **(F)** Quantification of cytosolic Ca^{2+} transients in astrocytic end-feet of wild-type (Ctrl), $Mfn2^{cKO}$ and $Mfn1^{cKO}$ astrocytes under the indicated conditions (n≥ 20 cells from 2-3 different mice per time and condition). **(G)** Frequency of cytosolic and mitochondrial Ca^{2+} transients within branches of $Mfn2^{cKO}$ astrocytes quantified utilizing the indicated sensors and under the specified conditions (n≥ 20 cells from 2-3 mice per time and condition). *, $p < 0.05$, **, $p < 0.01$, ***, $p < 0.001$ (non-parametric Mann-Whitney t-test).

Figure S6. Related to Figure 6. Assessment of cell proliferation in injured $Mfn2^{cKO}$ mice. **(A)** Example of reconstructed cortical vascular network following filament tracing (in white). Systematic inspection of the traced network led to the identification of potential artifacts (false segments, in yellow), which were corrected by manual selection and subsequent elimination.

Bar, 100 µm. **(B)** Top views of control and $Mfn1^{cKO}$ cleared cortices showing the extent of dextran-filled vasculature at 7 days post-SW. Arrowheads point to the lesion track. Insets depict zooms of the lesioned core region (circled in white). Bar, 200 µm. **(C)** Quantification of branch points, fractional volume and total length of the vascular network in $Mfn1^{WT}$ and $Mfn1^{cKO}$ cortices (n= 3-4 mice/condition; two-way ANOVA followed by Tukey's post-hoc test). **(D)** Pictures depicting large views of the injured cortex in $Mfn2^{WT}$ and $Mfn2^{cKO}$ mice at 7 days post-SW and following immunostaining for the nuclear marker SOX2 (labeling astrocytes) as well as EdU. Insets show co-localization of EdU with SOX2 (indicated by yellow arrowheads). Bar, 100 µm. **(E)** Quantification of total proliferating cells (upper graph) as well as proliferating astrocytes (SOX2+/EdU+) within the area surrounding the lesion track in $Mfn2^{WT}$ and $Mfn2^{cKO}$ mice at 7 days post-SW (n= 4-5 mice/condition; nonparametric Mann-Whitney t-test). **(F)** Fraction of endothelial (ERG+) as well as astrocytic (SOX2+) cells being double positive for EdU within the area surrounding the lesion track in $Mfn2^{WT}$ and $Mfn2^{cKO}$ mice at 7 days post-SW (n= 4-5 mice/condition; nonparametric Mann-Whitney t-test). *, $p < 0.05$, **, $p < 0.01$, ***, $p < 0.001$.

Figure S7. Related to Figure 6 and 7. Analysis of astrocytic mitochondrial morphology and Ca^{2+} dynamics following synthetic linker expression. (A) Examples of $Mfn2^{cKO}$ brain sections (obtained from $Mfn2^{lox/lox}$ x Glast::CreERT2 x $R26^{LSL\text{-}tdTomato}$) and corresponding control samples bearing tdTomato fluorescence in astrocytes. Brain sections were immunostained for the endothelial marker CD31 in order to reveal the vascular network at 7 days following SW-injury. Bar, 100 µm. **(B)** Zoom of reactive tdTomato+ astrocytes at 7 days post-SW in close proximity to the lesion. Pictures depict the polarized morphology of $Mfn2^{WT}$ and $Mfn2^{cKO}$ reactive astrocytes and a comparable extent of perivascular wrapping around the CD31+ vessels. Bar, 10 µm. **(C)** Quantification of astrocyte density within the injured cortices of $Mfn2^{WT}$ and $Mfn2^{cKO}$ tdTomato-expressing mice (n= 4 mice per condition; nonparametric Mann-Whitney t-test). **(D)** Quantification of perivascular mitochondrial fragmentation (i.e., fraction of perivascular fragmented mitochondria as calculated in Figure 2D) in $Mfn2^{cKO}$

astrocytes following transduction with AAV-ctrl or AAV-linker (n= 3 mice per condition; one-way Anova followed by Dunn's multiple comparison). **(E)** Scheme showing the AAV constructs utilized to express mitoGCaMP6f in tandem with OMM-mRFP-ER (or its control, OMM-mRFP) in astrocytes. **(F)** Experimental design showing AAV delivery followed by 2PLSM in slices and mitochondrial Ca^{2+} uptake analysis via AstroSparks. **(G)** Example of mitoGCaMP6-expressing $Mfn2^{cKO}$ astrocytes in brain slice transduced with either AAV-linker or AAV-ctrl and following AstroSparks processing and ROI analysis (ROIs in the end-feet are depicted in white, while the processes appear in red). Right panels depicts ROI traces and corresponding raster plots. Bar, 20 µm. **(H)** Quantification of the amplitude and duration of mitochondrial Ca^{2+} events in branches and end-feet of $Mfn2^{cKO}$ astrocytes transduced with the AAV-linker or AAV-ctrl (n≥ 29 cells per time and condition). **(I)** Analysis of branching points and total vessel length in CD31 immunostained brain sections obtained from $Mfn2^{WT}$ and $Mfn2^{cKO}$ injured mice (n= 3 mice/condition; nonparametric Mann-Whitney t-test). *, $p < 0.05$, ns, not significant.

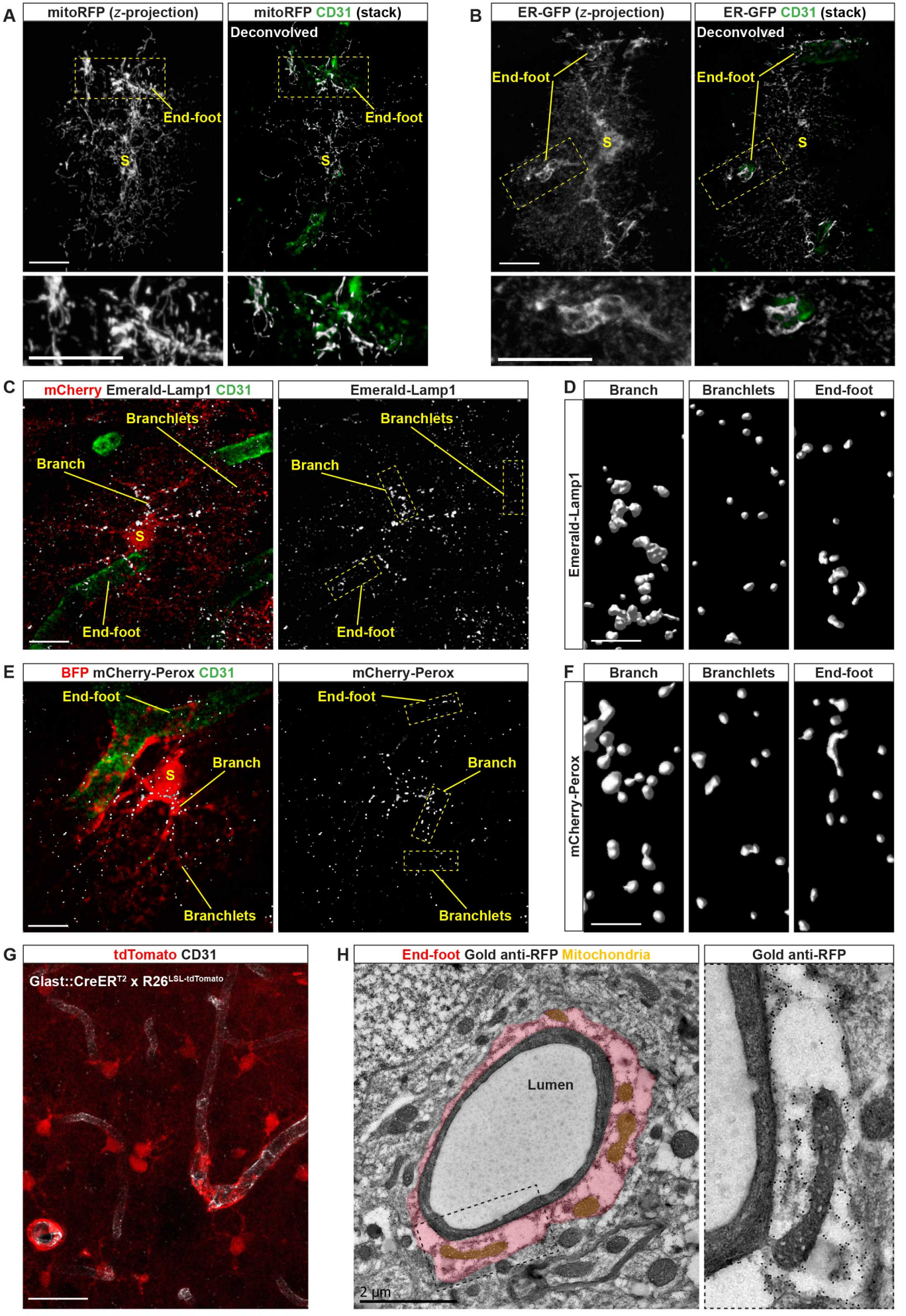
A
mitoRFP (z-projection)
mitoRFP CD31 (stack)
Deconvolved
End-foot
S
B
ER-GFP (z-projection)
ER-GFP CD31 (stack)
C
mCherry Emerald-Lamp1 CD31
Emerald-Lamp1
Branchlets
Branch
D
Branch
Branchlets
End-foot
Emerald-Lamp1
E
BFP mCherry-Perox CD31
mCherry-Perox
F
mCherry-Perox
G
tdTomato CD31
Glast::CreER^{T2} x R26$^{LSL\text{-}tdTomato}$
H
End-foot Gold anti-RFP Mitochondria
Gold anti-RFP
Lumen
2 µm

Figure S1

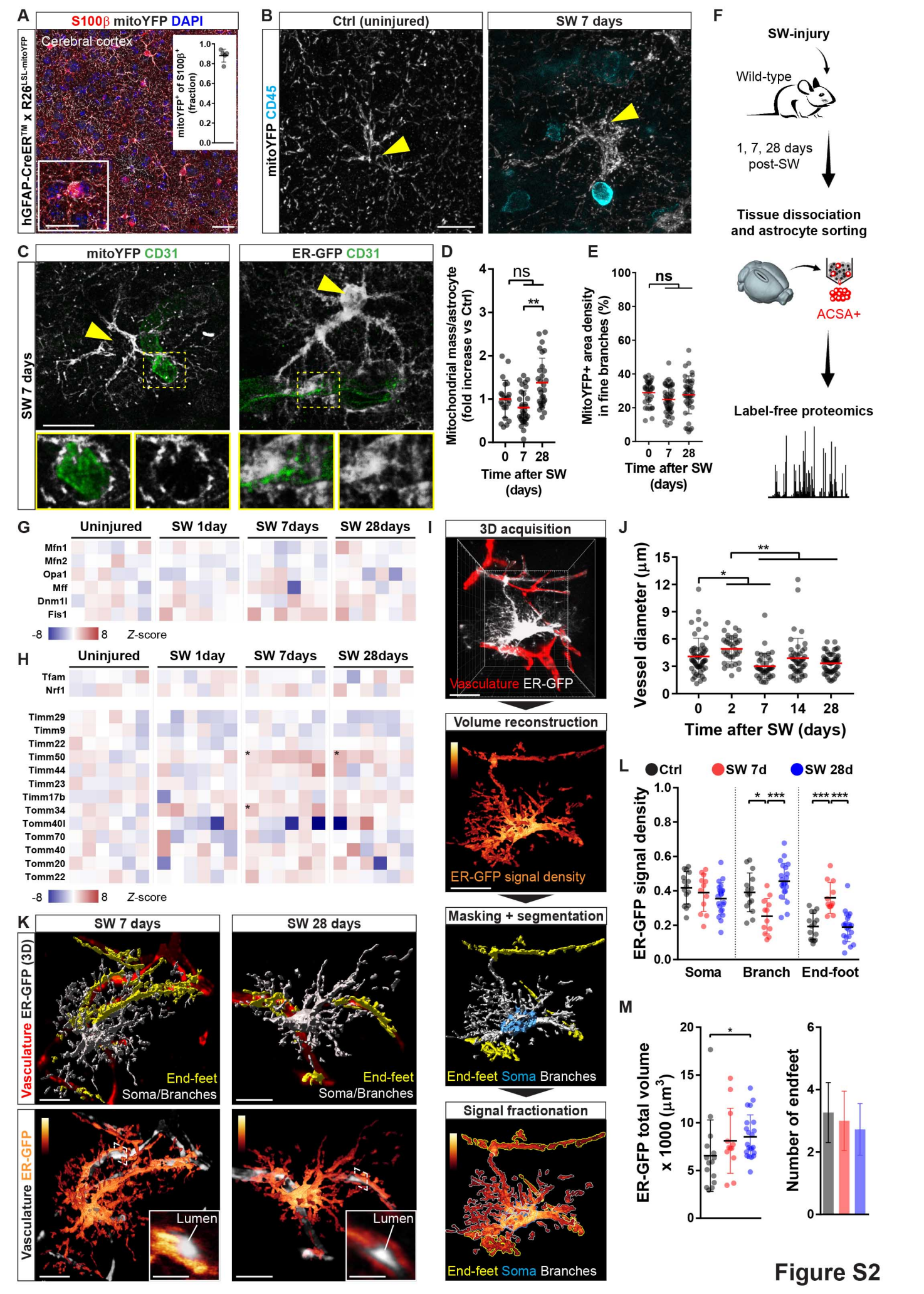
A
S100β mitoYFP DAPI
Cerebral cortex
hGFAP-CreER™ x R26LSL-mitoYFP
mitoYFP+ of S100β+ (fraction)
B
Ctrl (uninjured)
SW 7 days
mitoYFP CD45
C
mitoYFP CD31
ER-GFP CD31
SW 7 days
D
Mitochondrial mass/astrocyte (fold increase vs Ctrl)
ns
**
Time after SW (days)
E
MitoYFP+ area density in fine branches (%)
ns
Time after SW (days)
F
SW-injury
Wild-type
1, 7, 28 days post-SW
Tissue dissociation and astrocyte sorting
ACSA+
Label-free proteomics
G
Uninjured
SW 1day
SW 7days
SW 28days
Mfn1
Mfn2
Opa1
Mff
Dnm1l
Fis1
Z-score
H
Tfam
Nrf1
Timm29
Timm9
Timm22
Timm50
Timm44
Timm23
Timm17b
Tomm34
Tomm40l
Tomm70
Tomm40
Tomm20
Tomm22
Z-score
I
3D acquisition
Vasculature ER-GFP
Volume reconstruction
ER-GFP signal density
Masking + segmentation
End-feet Soma Branches
Signal fractionation
End-feet Soma Branches
J
Vessel diameter (µm)
Time after SW (days)
L
Ctrl
SW 7d
SW 28d
ER-GFP signal density
Soma
Branch
End-foot
M
ER-GFP total volume x 1000 (µm3)
Number of endfeet
K
SW 7 days
SW 28 days
Vasculature ER-GFP (3D)
End-feet
Soma/Branches
Vasculature ER-GFP
Lumen

Figure S2

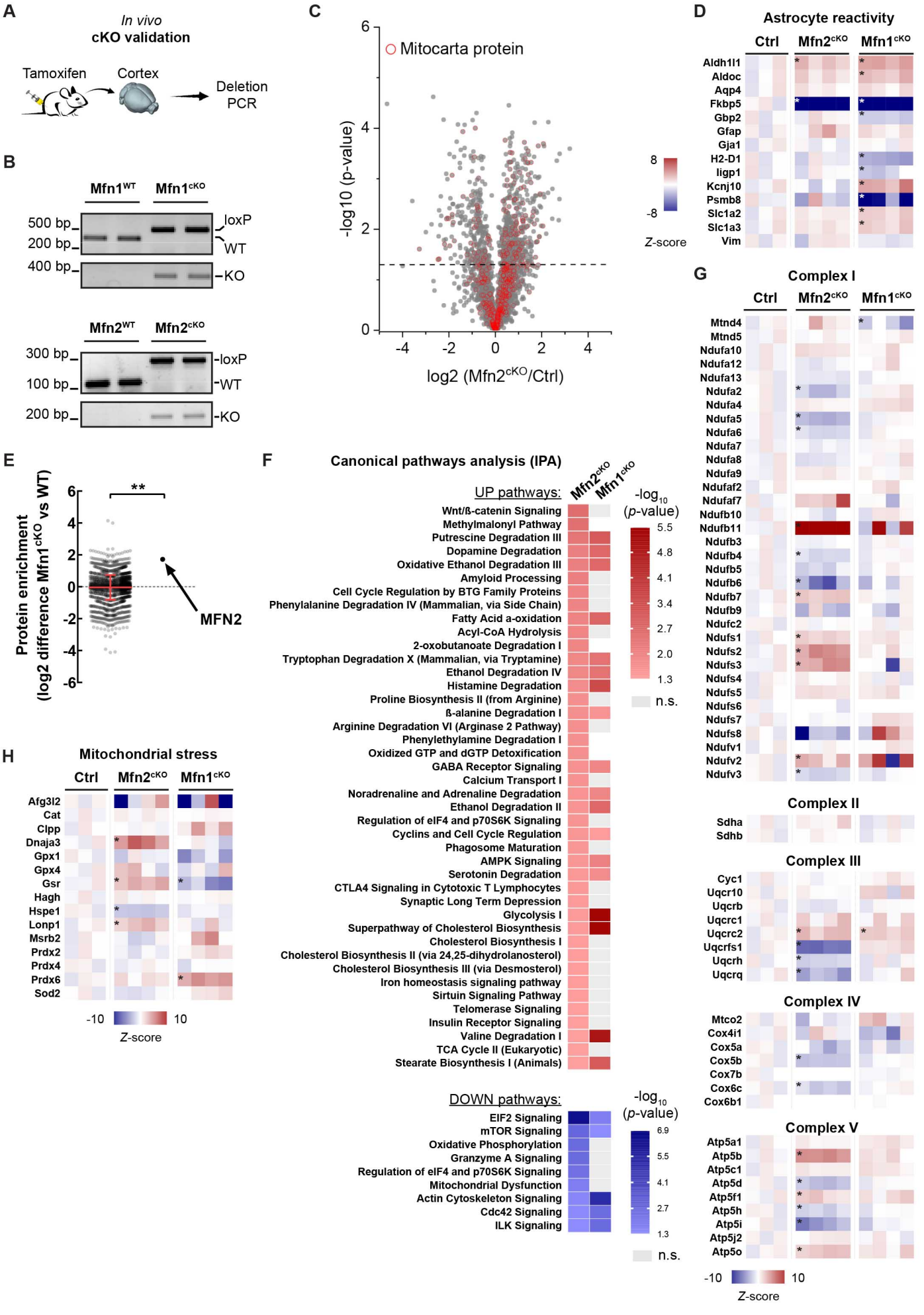
A
In vivo
cKO validation
Tamoxifen
Cortex
Deletion
PCR
B
Mfn1WT
Mfn1cKO
500 bp
200 bp
400 bp
loxP
WT
KO
Mfn2WT
Mfn2cKO
300 bp
100 bp
200 bp
loxP
WT
KO
C
Mitocarta protein
-log10 (p-value)
log2 (Mfn2cKO/Ctrl)
8
-8
Z-score
D
Astrocyte reactivity
Ctrl
Mfn2cKO
Mfn1cKO
Aldh1l1
Aldoc
Aqp4
Fkbp5
Gbp2
Gfap
Gja1
H2-D1
Iigp1
Kcnj10
Psmb8
Slc1a2
Slc1a3
Vim
E
Protein enrichment
(log2 difference Mfn1cKO vs WT)
**
MFN2
F
Canonical pathways analysis (IPA)
UP pathways:
Wnt/ß-catenin Signaling
Methylmalonyl Pathway
Putrescine Degradation III
Dopamine Degradation
Oxidative Ethanol Degradation III
Amyloid Processing
Cell Cycle Regulation by BTG Family Proteins
Phenylalanine Degradation IV (Mammalian, via Side Chain)
Fatty Acid a-oxidation
Acyl-CoA Hydrolysis
2-oxobutanoate Degradation I
Tryptophan Degradation X (Mammalian, via Tryptamine)
Ethanol Degradation IV
Histamine Degradation
Proline Biosynthesis II (from Arginine)
ß-alanine Degradation I
Arginine Degradation VI (Arginase 2 Pathway)
Phenylethylamine Degradation I
Oxidized GTP and dGTP Detoxification
GABA Receptor Signaling
Calcium Transport I
Noradrenaline and Adrenaline Degradation
Ethanol Degradation II
Regulation of eIF4 and p70S6K Signaling
Cyclins and Cell Cycle Regulation
Phagosome Maturation
AMPK Signaling
Serotonin Degradation
CTLA4 Signaling in Cytotoxic T Lymphocytes
Synaptic Long Term Depression
Glycolysis I
Superpathway of Cholesterol Biosynthesis
Cholesterol Biosynthesis I
Cholesterol Biosynthesis II (via 24,25-dihydrolanosterol)
Cholesterol Biosynthesis III (via Desmosterol)
Iron homeostasis signaling pathway
Sirtuin Signaling Pathway
Telomerase Signaling
Insulin Receptor Signaling
Valine Degradation I
TCA Cycle II (Eukaryotic)
Stearate Biosynthesis I (Animals)
DOWN pathways:
EIF2 Signaling
mTOR Signaling
Oxidative Phosphorylation
Granzyme A Signaling
Regulation of eIF4 and p70S6K Signaling
Mitochondrial Dysfunction
Actin Cytoskeleton Signaling
Cdc42 Signaling
ILK Signaling
-log10 (p-value)
n.s.
G
Complex I
Ctrl
Mfn2cKO
Mfn1cKO
Mtnd4
Mtnd5
Ndufa10
Ndufa12
Ndufa13
Ndufa2
Ndufa4
Ndufa5
Ndufa6
Ndufa7
Ndufa8
Ndufa9
Ndufaf2
Ndufaf7
Ndufb10
Ndufb11
Ndufb3
Ndufb4
Ndufb5
Ndufb6
Ndufb7
Ndufb9
Ndufc2
Ndufs1
Ndufs2
Ndufs3
Ndufs4
Ndufs5
Ndufs6
Ndufs7
Ndufs8
Ndufv1
Ndufv2
Ndufv3
Complex II
Sdha
Sdhb
Complex III
Cyc1
Uqcr10
Uqcrb
Uqcrc1
Uqcrc2
Uqcrfs1
Uqcrh
Uqcrq
Complex IV
Mtco2
Cox4i1
Cox5a
Cox5b
Cox7b
Cox6c
Cox6b1
Complex V
Atp5a1
Atp5b
Atp5c1
Atp5d
Atp5f1
Atp5h
Atp5i
Atp5j2
Atp5o
-10
10
Z-score
H
Mitochondrial stress
Ctrl
Mfn2cKO
Mfn1cKO
Afg3l2
Cat
Clpp
Dnaja3
Gpx1
Gpx4
Gsr
Hagh
Hspe1
Lonp1
Msrb2
Prdx2
Prdx4
Prdx6
Sod2
-10
10
Z-score

Figure S3

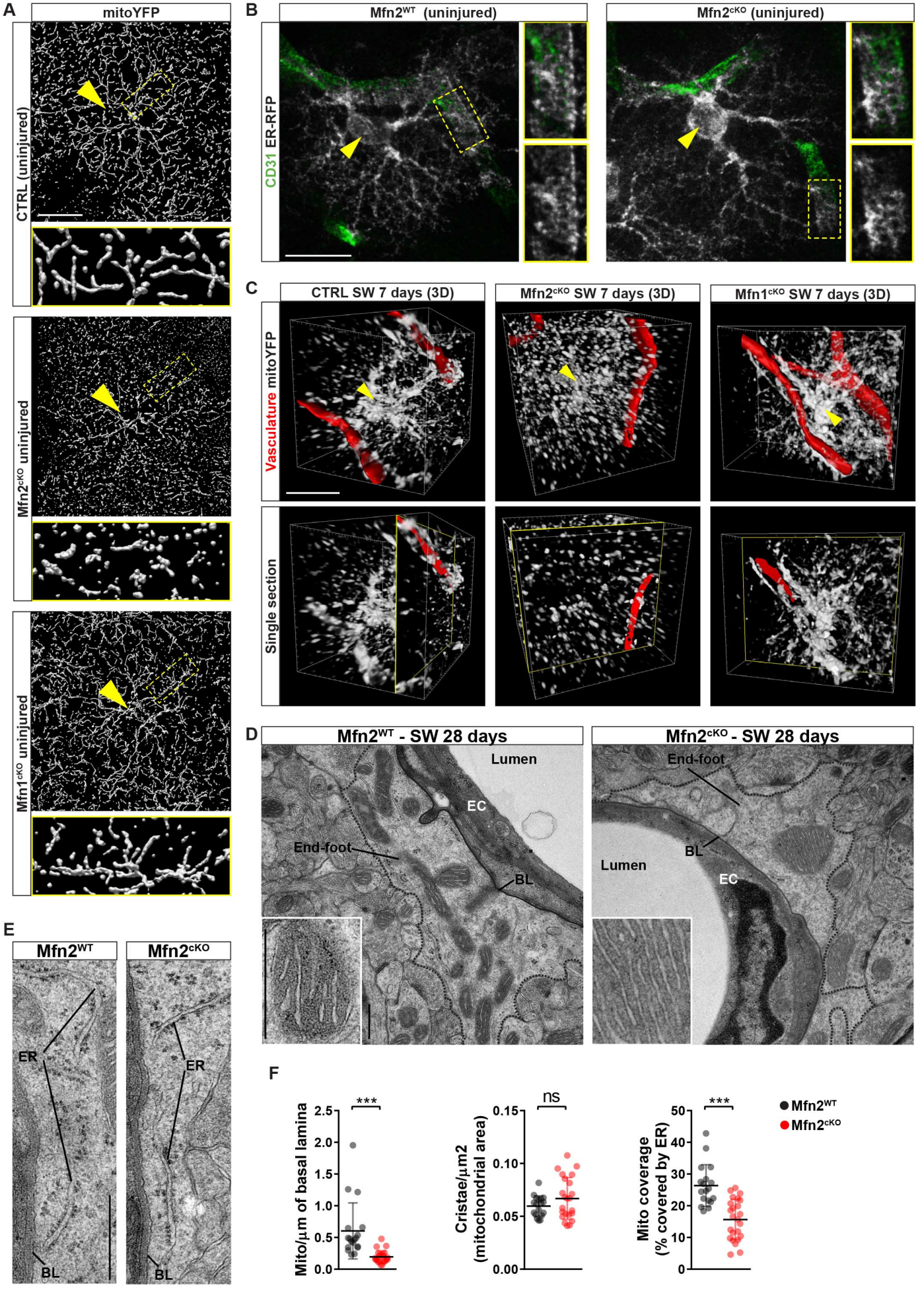
A
mitoYFP
CTRL (uninjured)
Mfn2cKO uninjured
Mfn1cKO uninjured
B
Mfn2WT (uninjured)
Mfn2cKO (uninjured)
CD31 ER-RFP
C
CTRL SW 7 days (3D)
Mfn2cKO SW 7 days (3D)
Mfn1cKO SW 7 days (3D)
Vasculature mitoYFP
Single section
D
Mfn2WT - SW 28 days
Mfn2cKO - SW 28 days
Lumen
EC
End-foot
BL
E
Mfn2WT
Mfn2cKO
ER
BL
F
Mito/µm of basal lamina
Cristae/µm2 (mitochondrial area)
Mito coverage (% covered by ER)
***
ns
Mfn2WT
Mfn2cKO

Figure S4

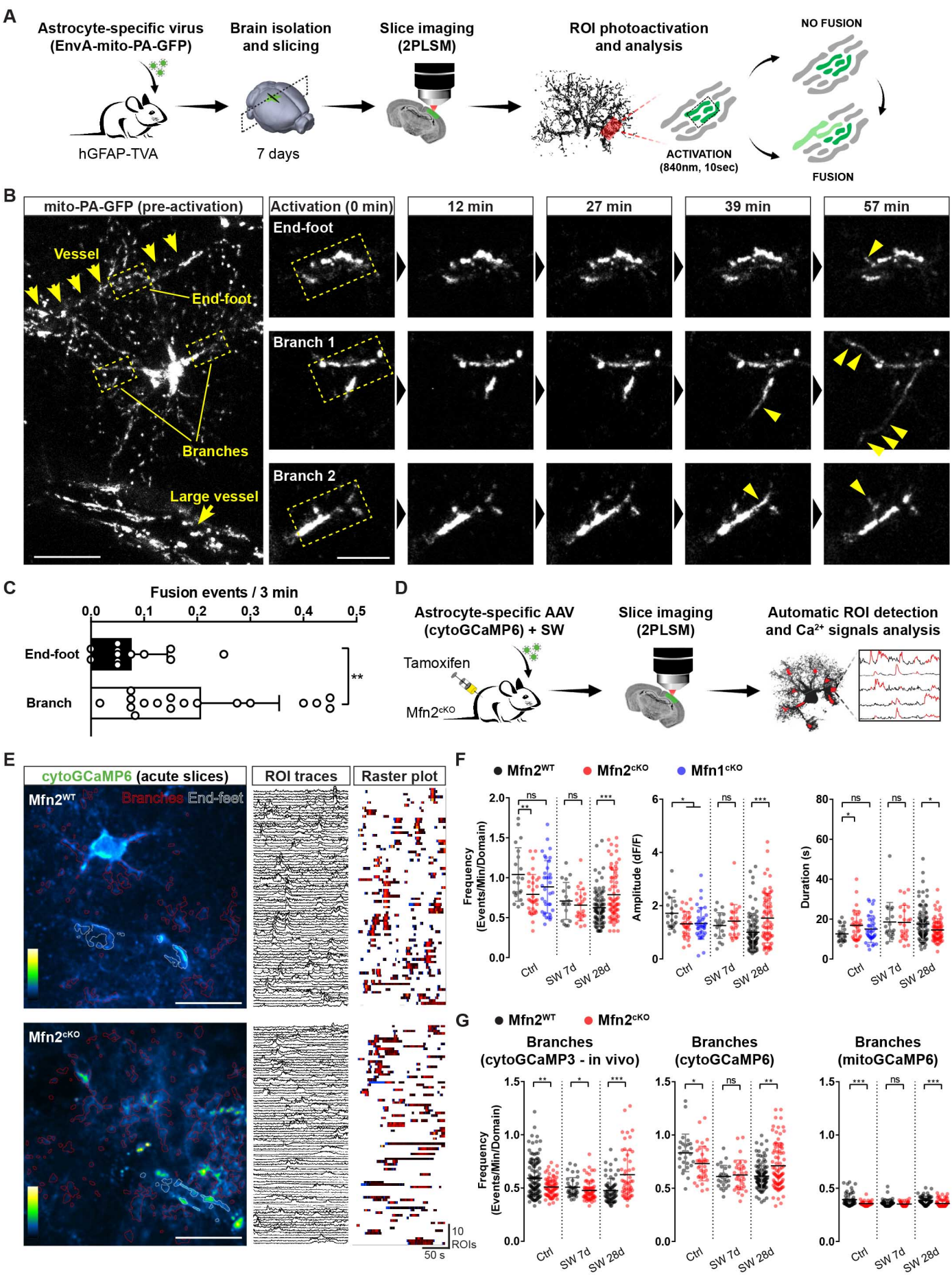
A
Astrocyte-specific virus (EnvA-mito-PA-GFP)
Brain isolation and slicing
Slice imaging (2PLSM)
ROI photoactivation and analysis
NO FUSION
hGFAP-TVA
7 days
ACTIVATION (840nm, 10sec)
FUSION
B
mito-PA-GFP (pre-activation)
Activation (0 min)
12 min
27 min
39 min
57 min
Vessel
End-foot
Branches
Large vessel
Branch 1
Branch 2
C
Fusion events / 3 min
0.0
0.1
0.2
0.3
0.4
0.5
End-foot
Branch
**
D
Astrocyte-specific AAV (cytoGCaMP6) + SW
Slice imaging (2PLSM)
Automatic ROI detection and Ca2+ signals analysis
Tamoxifen
Mfn2cKO
E
cytoGCaMP6 (acute slices)
ROI traces
Raster plot
Mfn2WT
Branches End-feet
Mfn2cKO
10 ROIs
50 s
F
Mfn2WT
Mfn2cKO
Mfn1cKO
Frequency (Events/Min/Domain)
Amplitude (dF/F)
Duration (s)
ns
Ctrl
SW 7d
SW 28d
G
Mfn2WT
Mfn2cKO
Branches (cytoGCaMP3 - in vivo)
Branches (cytoGCaMP6)
Branches (mitoGCaMP6)
Frequency (Events/Min/Domain)

Figure S5

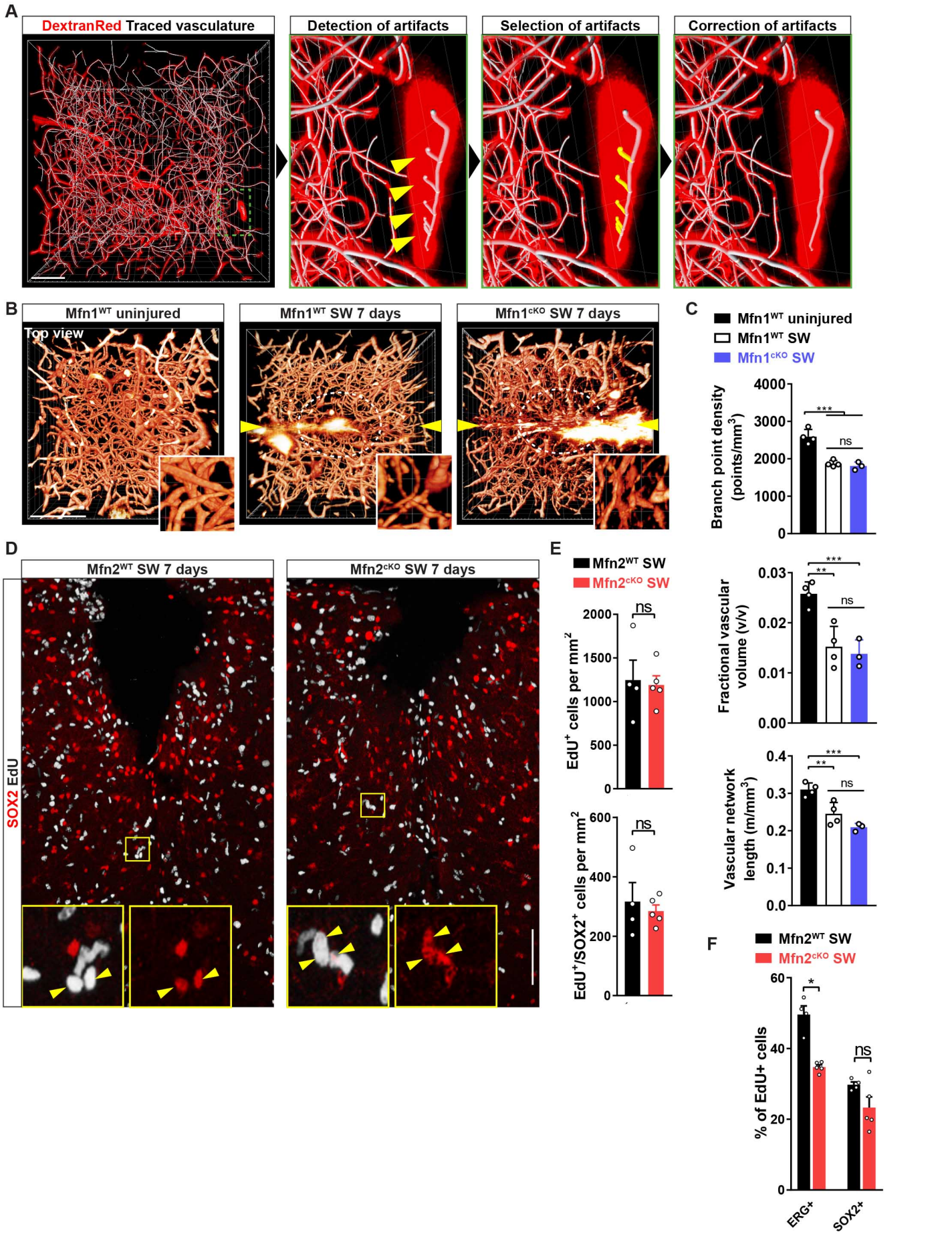
A
DextranRed Traced vasculature
Detection of artifacts
Selection of artifacts
Correction of artifacts
B
Mfn1WT uninjured
Top view
Mfn1WT SW 7 days
Mfn1cKO SW 7 days
C
Mfn1WT uninjured
Mfn1WT SW
Mfn1cKO SW
Branch point density (points/mm3)
4000
3000
2000
1000
0
***
ns
Fractional vascular volume (v/v)
0.03
0.02
0.01
0.00
***
**
ns
Vascular network length (m/mm3)
0.4
0.3
0.2
0.1
0.0
***
**
ns
D
Mfn2WT SW 7 days
Mfn2cKO SW 7 days
SOX2 EdU
E
Mfn2WT SW
Mfn2cKO SW
EdU+ cells per mm2
2000
1500
1000
500
0
ns
EdU+/SOX2+ cells per mm2
600
400
200
0
ns
F
Mfn2WT SW
Mfn2cKO SW
% of EdU+ cells
60
40
20
0
*
ns
ERG+
SOX2+

Figure S6

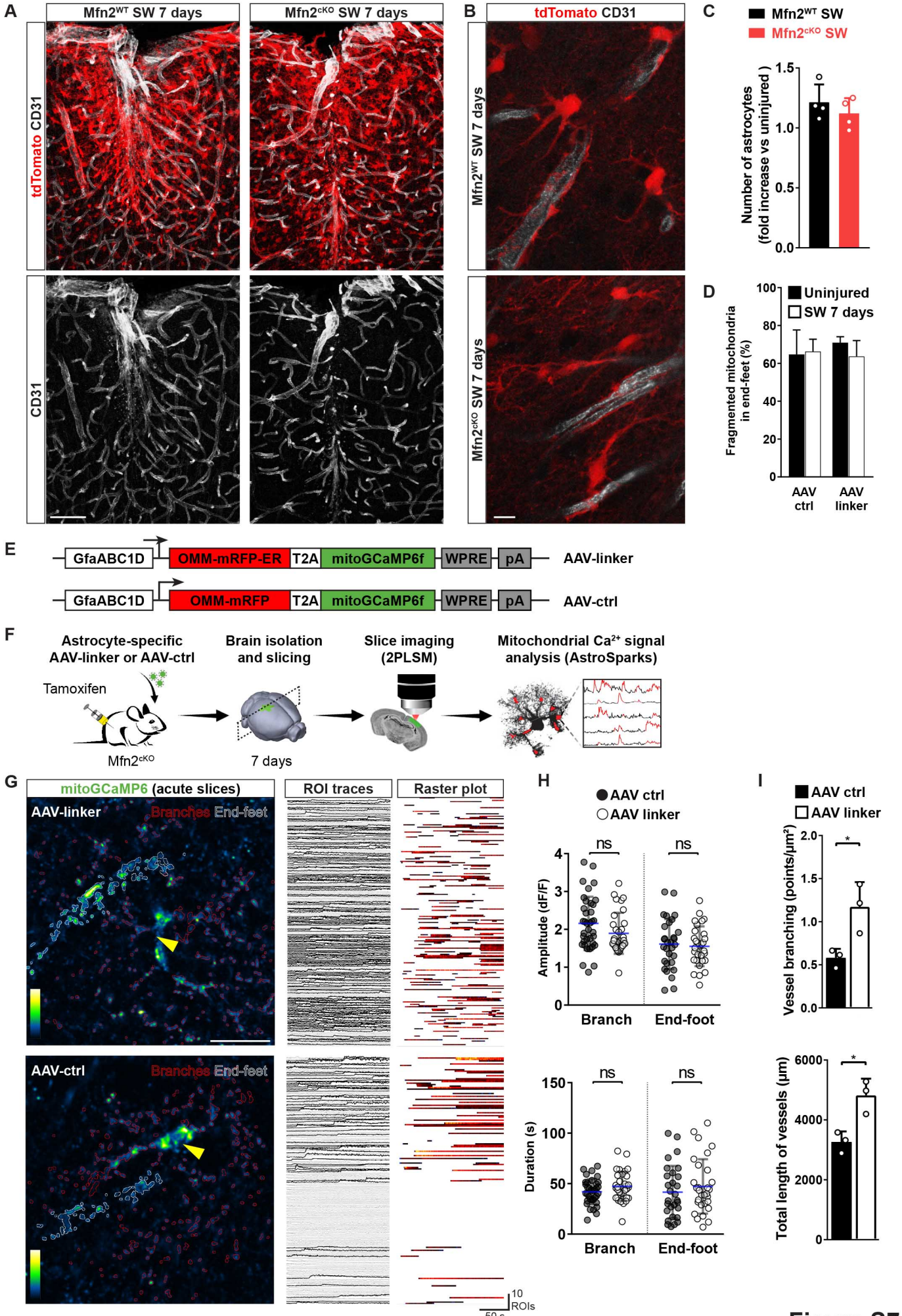
A
Mfn2WT SW 7 days
Mfn2cKO SW 7 days
tdTomato CD31
CD31
B
tdTomato CD31
Mfn2WT SW 7 days
Mfn2cKO SW 7 days
C
Mfn2WT SW
Mfn2cKO SW
Number of astrocytes (fold increase vs uninjured)
1.5
1.0
0.5
0.0
D
Uninjured
SW 7 days
Fragmented mitochondria in end-feet (%)
100
80
60
40
20
0
AAV ctrl
AAV linker
E
GfaABC1D
OMM-mRFP-ER
T2A
mitoGCaMP6f
WPRE
pA
AAV-linker
GfaABC1D
OMM-mRFP
T2A
mitoGCaMP6f
WPRE
pA
AAV-ctrl
F
Astrocyte-specific AAV-linker or AAV-ctrl
Brain isolation and slicing
Slice imaging (2PLSM)
Mitochondrial Ca2+ signal analysis (AstroSparks)
Tamoxifen
Mfn2cKO
7 days
G
mitoGCaMP6 (acute slices)
AAV-linker
Branches
End-feet
AAV-ctrl
ROI traces
Raster plot
10 ROIs
50 s
H
AAV ctrl
AAV linker
Amplitude (dF/F)
ns
Branch
End-foot
Duration (s)
I
AAV ctrl
AAV linker
Vessel branching (points/µm²)
*
Total length of vessels (µm)

Figure S7